The X-ray, Raman and TEM Signatures of Cellulose-Derived Carbons Explained

Petros Kasaira Mubari, Théotime Beguerie, Marc Monthioux, Elsa Weiss-Hortala, Ange Nzihou, Pascal Puech

C Journal of Carbon Research

MDPI

Article

The X-ray, Raman and TEM Signatures of Cellulose-Derived Carbons Explained

Petros Kasaira Mubari [1,2,*], Théotime Beguerie [2], Marc Monthioux [1], Elsa Weiss-Hortala [2], Ange Nzihou [2] and Pascal Puech [1,*]

[1] Centre d'Elaboration des Matériaux et d'Etudes Structurales (CEMES), CNRS, Université de Toulouse, 29 Rue Jeanne Marvig, CEDEX 04, 31055 Toulouse, France; marc.monthioux@cemes.fr

[2] IMT Mines Albi, UMR CNRS 5302, Centre RAPSODEE, Campus Jarlard, Université de Toulouse, CEDEX 09, 81013 Albi, France; theotime.beguerie@mines-albi.fr (T.B.); elsa.weiss@mines-albi.fr (E.W.-H.); ange.nzihou@mines-albi.fr (A.N.)

* Correspondence: petros.mubari@mines-albi.fr (P.K.M.); pascal.puech@cemes.fr (P.P.); Tel.: +33-(0)5-67-52-43-57 (P.P.)

Abstract: Structural properties of carbonized cellulose were explored to conjugate the outcomes from various characterization techniques, namely X-ray diffraction (XRD), Raman spectroscopy, and high-resolution transmission electron microscopy. All these techniques have evidenced the formation of graphene stacks with a size distribution. Cellulose carbonized at 1000 and 1800 °C at a heating rate of 2 °C/min showed meaningful differences in Raman spectroscopy, whereas in XRD, the differences were not well pronounced, which implies that the crystallite sizes calculated by each technique have different significations. In the XRD patterns, the origin of a specific feature at a low scattering angle commonly reported in the literature but poorly explained so far, was identified. The different approaches used in this study were congruous in explaining the observations that were made on the cellulose-derived carbon samples. The remnants of the basic structural unit (BSU) are developed during primary carbonization. Small graphene-based crystallites inherited from the BSUs, which formerly developed during primary carbonization, were found to coexist with larger ones. Even if the three techniques give information on the average size of graphenic domains, they do not see the same characteristics of the domains; hence, they are not identical, nor contradictory but complementary. The arguments developed in the work to explain which characteristics are deduced from the signal obtained by each of the three characterization techniques relate to physics phenomena; hence, they are quite general and, therefore, are valid for all kind of graphenic materials.

Keywords: cellulose; carbonization; disorder; Raman; XRD; crystallite size; HRTEM

Citation: Mubari, P.K.; Beguerie, T.; Monthioux, M.; Weiss-Hortala, E.; Nzihou, A.; Puech, P. The X-ray, Raman and TEM Signatures of Cellulose-Derived Carbons Explained. *C* **2022**, *8*, 4. https://doi.org/10.3390/c8010004

Academic Editor: Gil Goncalves

Received: 17 December 2021
Accepted: 30 December 2021
Published: 3 January 2022

1. Introduction

Carbonaceous materials derived from biomass have a wide range of applications, ranging from aqueous and gaseous pollutant adsorption [1,2] and catalysis [3–5], to energy storage [6,7]. The carbonization of a non-graphitizable material, such as cellulose, results in the formation of stacked graphenes lacking the long-range near-parallel extension (otherwise designated as the local molecular orientation (LMO)) [8], which is necessary for the solid to crystallize into genuine graphite. In this regard, there is some misinterpretation or confusion in the literature due to the fact that using a graphitization process (i.e., a heat-treatment above 2200 °C up to 3000 °C) does not compulsorily result in obtaining carbon materials with the structure of genuine graphite [9]. In the case of fully non-graphitizable carbons, only randomly oriented turbostratic carbons are obtained.

X-ray diffraction (XRD) patterns are routinely used for carbon characterization and provide parameters, such as L_c (average stack thickness perpendicular to the basal plane in the perfectly coherent domains, i.e., the crystallites) and L_a (average crystallite diameter in the basal plane) which are usually both calculated by the Scherrer equation through

the use of relevant peak widths. XRD also provides the lattice constants, a and c, which are usually indirectly calculated from the Bragg equation, which is made possible by calculating the period of a family of atomic planes and correlating it to the geometry of the crystal system. Additional correcting operations are required for small L_a and L_c, although it is nearly never mentioned in the literature [10]. An alternative is to use ad hoc functions obtained from the bottom-up approach [11]. For the turbostratic crystallites, increasing heat-treatment temperatures subsequently improves the stacking which is also accompanied by an increase in L_a, but this does not mean that there is a conversion into graphite. Characteristic features of non-graphitizable carbons include the prevalence of graphene curvatures, the presence of fullerene-like defects, short-distance misorientation between coherent domains, and, in the absence of catalysts, the impossibility to obtain graphite crystallites [12,13]. The aim of graphitization is to obtain graphite, meaning that the turbostratic stacks with inter-graphene spacing equal to or larger than 0.344 nm within a long-distance extended LMO must somehow be brought closer, down to 0.335 nm, as a consequence of the appropriate positioning of graphenes relative to each other within each crystallite. One important traditional way of measuring graphitization is by measuring the value of the spacing between graphene layers using the 2θ position of the $00l$ diffraction peaks in the XRD patterns [14].

With disordered graphenic materials, apparent sizes of the average crystallite determined by XRD, L_a and L_c, are usually used to denote the degree of order [14]. It was demonstrated by Oberlin [8], based on the previous assumption by Franklin [12], that the presence of cross-linking chemical functions in the organic precursor of non-graphitizable carbons hinders the alignment of polyaromatic molecules during primary carbonization (i.e., the early temperature-induced chemical transformation processes which drive the size of the local molecular orientation occurring below 600 °C). As a result, graphene stacks remain with small L_a and misoriented with respect to each other, which leads to graphitization resistance and subsequently determines the pore size.

In some poorly organised carbons, a peak may appear below the inter-graphene diffraction peak at 2θ~20–26°, typically at 2θ~10–13° (values for a Cu X-ray source) [15]. XRD has widely been used in the literature to account for stacking disorder, with stacking faults being defined as the absence of ABAB (Bernal) stacking. The crystallite dimensions in the z direction are reduced accordingly, and in turn, the resulting XRD peaks will broaden.

Raman spectroscopy is another well-established, non-destructive technique which is used to acquire information pertaining to the bulk properties of polycrystalline materials [16–19]. The crystallinity of carbon materials has been increasingly determined by Raman spectroscopy as an alternative to XRD [20]. Graphenic materials exhibit a Raman peak related to the sp^2 C bonding energy, known as the G band, which appears at 1580 cm^{-1}, corresponding to the position for the regular graphite structure. The D band observed around 1350 cm^{-1} in less ordered carbons is mainly associated with point defects and domain edges. While efforts have been made to reconcile XRD and Raman spectroscopy, results have not always been conclusive. During the pyrolysis of wood, Zickler et al. [21] concluded that the estimate of the graphenic crystallite size L_a derived from its correlation with the I_D/I_G ratio, as proposed by Tuinstra and Koenig [19], must be taken with caution. Indeed, not only was it not applicable for $L_a < 2$ nm, as previously stated by Ferrari and Robertson [22], but significant mismatches can also be seen for large L_a due to the ways through which the Raman spectra are exploited [21]. Furthermore, laser power effects [23], which can be material-dependent [24], as well as order/disorder differences between different carbon materials, are expected to also have an impact on Raman spectroscopy results in this first-order region. Besides intensity, both the position and width variations of the Raman D and G bands are also used to determine the degree of structural order [25]. For this purpose, it is a common practice to adopt a five-band decomposition procedure to fit the Raman spectra [20,26–29] and extract tiny shape variations of the Raman spectrum (decomposition is a term definitively better than deconvolution as the number of peaks and the way of proceeding are empirical). The literature dealing with Raman spectroscopy

provides other parameters which aim to describe carbon materials. However, this is dependent on the sample type. Therefore, establishing a universal characterisation method is impossible as the texture, nanotexture, and structure (see our definitions of these terms in the "Methods" section) may vary significantly from one carbon material to another.

As a usual complement to Raman spectroscopy and XRD, high-resolution transmission electron microscopy (HRTEM) has been a useful technique for investigating carbon materials at the nanoscale, and tentatively obtaining quantified parameters describing the degree of order, mostly based on lattice fringe imaging [8,30,31]. HRTEM is used to obtain information on the texture, nanotexture, and structure of carbonaceous materials, but is prone to artefacts and intense labour, and is too local for some of the issues to be addressed. Furthermore, when dealing with bulk materials, such as chars, only the graphenes oriented edge-on can be revealed with sufficient contrast, and the fact that HRTEM images are 2D projections of 3D samples is likely to induce misinterpretations of the images.

In this paper, XRD, Raman spectroscopy, and HRTEM are used to study the texture, nanotexture, and crystalline structure of cellulose-derived chars carbonized in the 1000–1800 °C range. It is not of common knowledge that, despite the parameter name being the same, these techniques do not measure the same L_a. It is, therefore, important to compare and discuss what the differences are. First, we outline the techniques used to analyze the samples and the parameters of interest which were used to account for the carbon material organization. Then, we describe the theoretical aspects used to model and calculate the diffraction patterns. Finally, the nanotexture, texture, and structure of the cellulose-derived carbons are described, including the average crystallite sizes, in full agreement with the simulated XRD profiles, the experimental XRD patterns, Raman data, and HRTEM results.

2. Experimental

2.1. Materials, Treatments, and Terminology

Microcrystalline cellulose [CAS: 9004-34-6] was obtained from Sigma Aldrich Chimie S.a.r.l (Saint Quentin Fallavier, France). The carbonized samples were produced following a two-step process. First, 10 g of raw cellulose were pyrolyzed under N_2 with a flow rate of 1 L/min in a Carbolite tubular furnace at a temperature of 800 °C using a heating rate of 2 °C/min. A one-hour isotherm was applied. The resultant chars were collected after cooling and were subjected to further pyrolysis at 1000 °C and 1800 °C in a Nabertherm tubular furnace under a 5 L/min N_2 stream using a heating rate of 2 °C/min. The initial pyrolysis step serves the purpose of removing tars to prevent the clogging of the high-temperature furnace.

We chose 2 samples and annealed them at very different temperatures. 1000 and 1800 °C heat-treatment temperatures were chosen because they are both milestone temperatures, as far as carbonization processes are concerned. The former is in the temperature range where most of the remaining hydrogen atoms (as aromatic -CH) are released, and corresponds to the "coke" stage in industrial processes. The latter is in the range of the end of the secondary carbonization, beyond which graphitization processes may start (regardless whether they will succeed). In our previous studies on graphitizable carbons [11], the differences in terms of crystallite size between these 2 temperatures were really important. In particular, at an annealing temperature of 1800 °C, AB pairs began to form.

To describe the inner organization of graphenic materials, we used a three-term description where all terms were exclusive: the texture describes how graphene stacks are arranged with respect to each other at long distance; the imperfections (curvatures, defects) of the graphene layers determine the nanotexture; and the structure encompasses the diverse ways in which the graphenes pile up within a crystallite, among which the most common configurations are turbostratic, Bernal graphite, and rhombohedral graphite. More details are provided in Monthioux et al. [32].

2.2. X-ray Diffraction

XRD diffraction patterns were recorded from the carbonized cellulose samples on a Bruker RX-D8 Advance X-ray diffractometer with a non-monochromated Cu K_α radiation source (average λ = 1.5406 Å). The domains which scatter the X photons in a coherent manner represent the crystallites. Raw diffractograms exhibit an intense background, presumably due to a variety of X-photon interactions with the matter (Compton effect, absorption, polarization, etc.). Hence, they were treated for removing the background using continuously decreasing functions, which is a routine procedure for X-ray pattern analysis. The resulting diffraction profiles obtained from experiments were fitted using a pseudo-Voigt function for the peaks appearing at $2\theta \approx 13^\circ$ and $2\theta \approx 24^\circ$, and specific parameterized functions were used for the peaks at $2\theta \approx 43^\circ$ and $2\theta \approx 80^\circ$ in MATLAB® [11]. This was completed in accordance with the Rietveld method, and the theoretical line profiles were refined by non-linear least-squares until a measured diffraction line profile was matched [33]. The interplanar spacing was calculated using the $2\theta \approx 24^\circ$ peak position labelled *001*. We decided to use this notation *001* because the material remained turbostratic, whereas both *002* and *003* were only valid for the Bernal and rhombohedral graphite structures, respectively. However, it must be kept in mind that these 3 notations all correspond to the intergraphene spacing. We also proceeded to calculate the periodicity associated with the peak at $2\theta \approx 13^\circ$, which will be named the Non-Identified (NI) peak, as a start. One can note that the NI peak is still present with Co sources (1.789 Å), allowing us to eliminate the artefact hypothesis. The graphenic crystallite sizes L_c were directly obtained from the Scherrer equation applied to the *001*. L_a (pertaining to the *10* asymmetric band for turbostratic carbons) and were obtained as a parameter of the parametrised function. Examples of the functions used are included in the supplementary information of ref. [11]. While a simple Gaussian function accounts well for the *001* peak, more specific functions are necessary for fitting the *10* and *11* bands. In these functions, L_a is the only adjustable parameter (if we do not consider intensity). Thus, using the classical approach, which is based on the Scherrer equation, a complex user-dependent fit, and the shape factor K, is no longer necessary for fitting these two peaks with our approach.

2.3. Modelling the X-ray Diffraction Peak at $2\theta \approx 13^\circ$

The various defects (only one will be reported here) and stacking configurations were modelled by first constructing crystallite models with MATLAB®, and then by calculating the related X-ray diffractograms using the highly parallelized XaNSoNS freeware [34] with the ultimate goal to find a diffractogram that matches the experimental profiles.

2.4. Raman Spectroscopy

Raman spectroscopic analysis of carbonized cellulose was performed with an XploRA Plus spectrometer using a low laser power (1.4 mW), an objective of magnification ×50, and laser wavelengths/energies of 638 nm/1.94 eV (red) and 532 nm/2.33 eV (green) considering an acquisition time of 100 s. The laser spot size was larger than 1 µm and no heating was observed. We used two approaches to interpret the Raman spectra. In the first approach, we fitted the experimental spectra with a D band which was decomposed in two contributions and a G band for obtaining accurate values for the respective intensities as well as the linewidths. In the second one, we fitted the spectra with five bands corresponding to a spectral decomposition often used in carbon material characterization.

2.4.1. Fitting Procedure and Parameters When Considering the D and G Bands Only

The usually symmetric D band was fitted with two Voigt functions, a sharp one D_s, and a broad one D_b, located at the same spectral position, and a combination of Gaussian and Fano functions was used for fitting the G band [35]. The parameters of interest are the ratio of the intensities of the D and G bands (I_D/I_G) and the full width at half maximum of the D band ($FWHM_D$), which will be used to estimate L_a. Table 1 outlines the parameters that were of interest after fitting the experimental spectra with two bands. The crystallite size L_a

was calculated in three ways by exploiting Tuinstra–Koenig's correlation for L_a > 2 nm [19], the Ferrari's and Robertson's law for L_a < 2 nm [22], and the confinement model also for L_a larger than ~2 nm [36].

Table 1. Extracted parameters for the D and G band-fitted Raman spectra.

Extracted Parameters	Significance
(I_D/I_G)	Calculation of L_a [19,22]
D band—$FWHM_D$	Calculation of L_a [36]
D band	Degree of graphenic-sp^2 disorder

Laser energy dependencies were accounted for by taking into consideration the following relation [18]:

$$\frac{I_D}{I_G} = \frac{f(La)}{E_L^{\alpha}} \quad (1)$$

It is expressed as a function of the crystallite size $f(L_a)$, where (I_D/I_G) represents the intensity ratio and E_L is the laser energy whilst α is the exponent to be calculated. α = 4 for graphite [37] but for poorly organized carbon, this value decreases [35], although it always stays positive.

After considering the laser energy dependencies, L_a from the Tuinstra–Koenig correlation is given by (L_a > 2 nm):

$$L_a = \frac{4.4}{\left(\frac{I_D}{I_G}\right)} \times \left(\frac{2.41}{EL}\right)^{\alpha} \quad (2)$$

L_a from the Ferrari's and Robertson's law is given by (L_a < 2 nm):

$$L_a = \sqrt{\left(\frac{\left(\frac{I_D}{I_G}\right)}{0.55 \times \left(\frac{2.41}{EL}\right)^{\alpha}}\right)} \quad (3)$$

while I_D/I_G is expected to be maximum around 2 nm.

L_a from the confinement model is given by ($L_a \geq 2$ nm):

$$L_a = \frac{580}{FWHM_D} \quad (4)$$

with a continuous variation without notable change at L_a = 2 nm (for small L_a, the 580 coefficient decreases, allowing to find a higher limit value).

2.4.2. Fitting Procedure and Parameters When Considering Five Bands

The idea of having several bands for the fitting means having correlations which aim to determine the degree of disorder and the amorphous content. Usually, the functions (Gaussian, Lorentzian, Voigt) and the fixed parameters (usually wavenumbers) are selected to reveal the consistent shape variation of the Raman spectrum within a family of samples, while the background is often removed first. The experimental Raman spectra were decomposed into five bands in a manner summarized in Table 2.

Table 2. Consensual attribution from the literature and corresponding functions that were used for the fitting of Raman spectra with five bands [20,28,38,39].

Bands and Usual Position in Graphenic Materials (cm^{-1})	Fitting Function	Representation
G ≈ 1580	Voigt	sp^2
D_1 ≈ 1350	Voigt	defects in sp^2 (point defects, edges, curvature)
D_2 ≈ 1620	Gaussian	defects in sp^2, needed due to fixed G band wavenumber and thus associated to disorder
D_3 ≈ 1500	Gaussian	amorphous carbon

To quantify both the disorder degree and amorphous content, we used the intensity ratio of the D_3 band to the total intensity of all the bands $\frac{ID_3}{I_{total}}$. As the shapes of our experimental spectra varied with the treatment temperature as well as in function of the excitation energy used, for consistency, we opted for a Voigt shape (a combination of Lorentzian and Gaussian shapes) in some regions and a Gaussian shape in other regions.

2.5. HRTEM Micrographs, Image Filtering Analysis, Fringe Analysis

HRTEM images of the samples were collected using a SACTEM FEI TECNAI F20 microscope. This microscope, equipped with a field emission gun (Schottky type), was Cs-corrected (objective lens) and operated at 100 kV.

The image filtering using Fourier transform was used to extract information relative to the different domains from HRTEM images for some particular spatial frequencies, i.e., corresponding to the intergraphene distance of 3.4 ± 0.2 Å.

No value regarding the average fringe length, either straight or continuous but curved, was extracted from the HRTEM study because values would be biased by the projection effect already mentioned in the introduction section (unless domains are large, which is not the case with our samples). Indeed, projecting lattice fringes from a 3D volume onto a 2D imaging device is likely to generate fringe lengths shorter than they actually are, depending on the actual fringe lengths and the degree of textural and nanotextural anisotropies. One way to tentatively limit this could be to prepare sample TEM specimens as thin as possible, but then the fringe length could be physically altered by the preparation method.

3. Results and Discussion

3.1. X-ray Diffraction

Figure 1a,b present the raw XRD patterns (including the background, abbreviated with bg) for the cellulose carbonized at temperatures 1000 and 1800 °C. An intense background is seen at low scattering angles; hence, it is a routine in XRD analysis to merely subtract it, as mentioned is Section 2.2, in order to enhance the scattered peaks from the material. The bottom profile in Figure 1a,b show the result from the subtraction. Four broad peaks appear at around 13°, 24°, 43°, and 80°, corresponding to the NI peak, the intergraphene distance, and the *10* and *11* Laue indices of the in-plane atomic periodicities in isolated or turbostratically stacked graphenes, respectively.

At first glance, the two XRD profiles of the carbonised cellulose samples in Figure 1 differ in the background intensity, and differ slightly in the intensity, width, and positions of the peaks upon the temperature increase. Employing the Bragg's law ($2.d.\sin(\theta) = n.\lambda$) for the d_{001} peak at ~24°, an intergraphene distance after correction [10] of 3.68 Å was found for the cellulose char at 1000 °C and of 3.55 Å for the cellulose char at 1800 °C. The decrease in the intergraphene distance signifies an improvement in the material nanotexture (Table 3). It is worth noting that the decrease in the I_{bg}/I_{001} ratio from 1.65 to 0.87 is consistent with the assignment of at least part of the background to disorder, as claimed by [40], as it is expected that disorder decreases as the carbonization temperature increases.

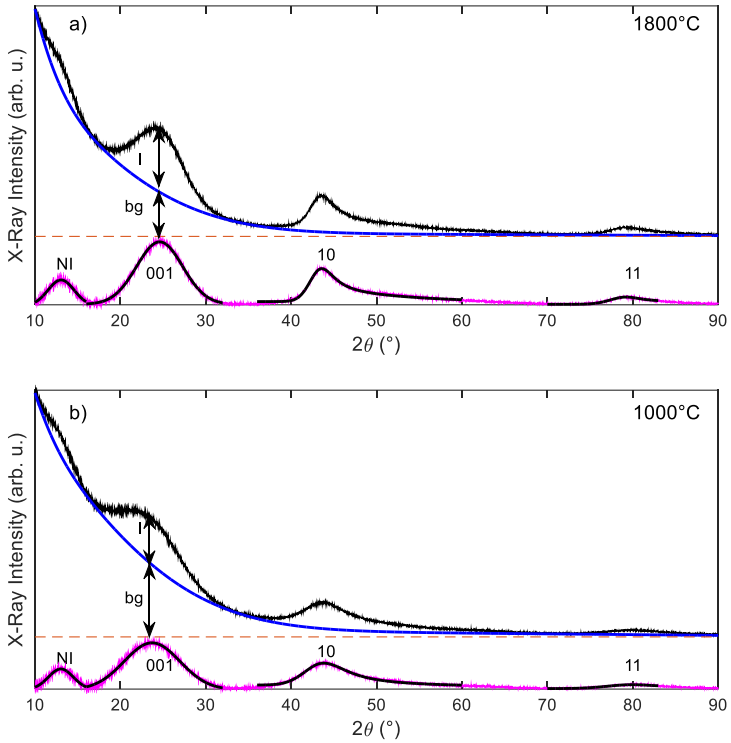

Figure 1. Raw and fitted X-ray diffraction profiles after background removal for cellulose-derived carbons obtained at (**a**) 1800 °C and (**b**) 1000 °C at a heating rate of 2°/min. Black curves for the diffractograms without background are the resulting fitting lines, obtained by the method described in [11].

Table 3. XRD parameters for cellulose-derived carbons at different carbonization temperatures. * From the Bragg's law without correction, corresponding to the apparent intergraphene spacing, ** with correction corresponding to the true intergraphene spacing (see [10]).

Extracted Parameters	Treatment Conditions	
	1000 °C, 2 °C/min	1800 °C, 2 °C/min
L_c(nm) from *001*	1.04	1.26
L_a (nm) from *10*	1.85	3.22
L_a (nm) from *11*	1.76	2.85
d_{001} (Å)	3.75 * (3.68 **)	3.62 * (3.55 **)
$a_{C=C}$ (Å)	1.42	1.42
$FWHM_{NI}$ (°)	3.46	3.46
$\frac{FWHM_{NI}}{FWHM_{001}}$	0.44	0.54
$\frac{A_{NI}}{A_{001}}$	0.20	0.21
$\frac{I_{NI}}{I_{001}}$	0.44	0.39
$\frac{I_{bg}}{I_{001}}$	1.65	0.87

These values are consistent with reports in the literature for biomass-issued carbons [41–43]. While the peak intensities do not increase significantly, the crystallite sizes L_c and L_a increase with increasing the carbonization temperature from 1000 °C to 1800 °C, although moderately for L_c and more extensively for L_a. L_c corresponds mainly in both cases to stacking of three carbon layers (we consider the van der Waals limit). This indicates the expected gradual increase in the dimensions of the turbostratic carbon crystallites with temperature, which mostly occur by gradually merging the crystallites into larger ones thanks to the progressive healing of the peripheral defects and the resulting slight misorientations which affect the crystallites [8].

On the contrary, the width of the peak at 13° remains constant ($FWHM_{NI}$ in Table 3). Despite being intense and single, this peak does not correspond to any periodicity in the graphite structure or its degenerative, turbostratic structure. However, it is striking that, with perfect graphite, the length of the unit cell along c is 6.7 Å, i.e., it could give a position at 2θ = 13°. However, of course, it is known that, in the graphite unit cell, the first graphene plane is in phase opposition to the second, leading to destructive interference and no intensity; hence the first scattered intensity appears for twice the 2θ value (corresponding to the *002* peak). Said otherwise, in graphite, the diffraction peak accounting for the (*001*) plane family is not a *001* peak at ~13° but a *002* peak at ~25°, because the unit cell is multiple and involves two equally spaced graphene layers instead of one. This suggests several possible origins for the NI peak: (i) a structural defect for which the middle graphene plane is missing in the cell, or a specific graphene configuration; (ii) the persistence of a structural, periodic feature specific to cellulose; and (iii) a specific feature of the XRD signal, when generated by poorly organized carbon, mostly made of tiny graphene stacks. Modelling was then performed to check two of these hypotheses whereas the others will be just discussed, as follows.

A plausible defect is that of inter-locked graphene sheets exhibiting curvatures as shown in Figure 2a, which is a quite common dislocation figure in graphene-based materials of any kind, including graphite. A peak below the d_{001} peak is present and is called in the following the defect peak (DP) (see Figure 2a). However, should this type of dislocation be the only responsible for the NI peak, the decrease in the intergraphene spacing (upshift of the *001* 2θ position in Figure 1) when carbonizing from 1000 to 1800 °C should also induce an upshift of the NI peak 2θ position, which is not observed. Moreover, the FWHM of the calculated DP peak obtained is not consistent with the experimental diffractograms.

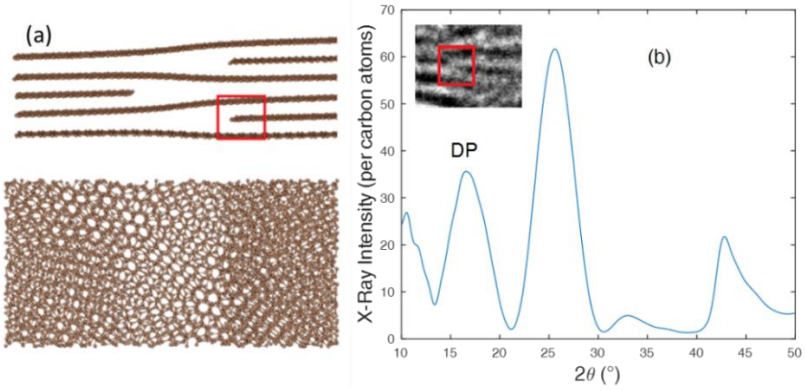

Figure 2. (**a**) Modelled dislocation showing an example of such a defect. (**b**) Simulated diffraction pattern profile obtained from the framed area in the atomistic model in (**a**), with an inset of a corresponding lattice fringe TEM image observed in a defective carbon.

Graphene edges connected or folded while forming loops are able to provide such a constant periodicity whatever the intergraphene distance, as ~6–7 Å corresponds to the diameter of the resulting channel. However, such a graphene termination is not observed in graphenic carbons obtained from the regular carbonization of organic precursors, and corresponds to specific process conditions instead [44].

Another hypothesis to consider could be that the 13° peak accounts for a remaining periodic feature of the cellulose skeleton. Indeed, XRD patterns of pristine (uncarbonized) cellulose do exhibit such a periodicity [45]. Unfortunately, modelling the full carbonization process of cellulose is impossible as it would require unrealistic computer time; hence, only the first steps are reported in the literature [46]. Nevertheless, the removal of atoms through the release of CO, CO_2, and H_2O, during primary carbonisation (i.e., <600 °C) and subsequent polyaromatization during secondary carbonization, should destroy this periodicity. Accordingly, it has been observed that the features corresponding to cellulose disappear [47]. Generally speaking, no such a persistence of an atomic-scale feature from the

original organic skeleton upon carbonization was ever observed in the literature, whatever the precursor.

Finally, a peak around 2θ = 13° was also evidenced for poorly organized carbon materials originating from precursors other than cellulose [48,49]. This suggests that the 13° peak is somehow associated with diffraction patterns from poorly organized carbons rather than specific to a cellulose origin. Consequently, we simulated the diffraction patterns for small graphene stacks (turbostratic) with L_a = 0.7, 1, 2, and 3 nm, with the number of layers ranging from 1 to 5 (see Figure 3). From the various modelled spectra reported in Figure 3, we can make several statements:

- Single graphenes generate a large intensity at a low 2θ angle whatever L_a, rapidly decreasing as the scattering angle increases. This is consistent with a recent statement from the literature, which showed that poorly organized carbon is able to contribute significantly to the background, specifically at low angles [40]. Therefore, our modelling supports this statement, and identifies that such a contributing intensity profile at low angles reveals the occurrence of individual graphenes.
- For an odd number (here 3 and 5) of turbostratically stacked layers with L_a in the range 1–2 nm, a peak shows up in the 13° range, resulting from interference effects. The position of this peak is dependent on L_a. Stacks involving an even number of graphenes (here 2 and 4) do not exhibit this peak, meaning that, in this case, interferences are destructive. This destructive effect rapidly vanishes as the number of graphenes in the stacks increases beyond 5.
- The actual *001* peak resulting from the stacking periodicity shift towards lower angles (from ~25.5 to ~22°) while the number of graphenes in the stack decreases (here from 5 to 2), as shown by Fujimoto [10], despite the fact that the intergraphene distance remains the same in our simulation.
- With ultra-small L_a (<1 nm), intensity is generated at a low 2θ angle which can significantly contribute to the background.

From all the possibilities explored in Figure 3 and using the corrected d_{001} values for 1000 and 1800 °C from Table 3, in Figure 4, we reported the calculated diffraction patterns with L_a = 1 nm and three layers. Indeed, the matching between the simulated and experimental 13° peaks is perfect. The $FWHM_{NI}$ of the simulation equals 3.79°, which is very close to the experimental value of 3.46° (see Table 3). This is definitely the only simulation giving such a small value. The ratio of the simulated peak areas A_{NI}/A_{001} equals 0.38. On the other hand, the matching is not good in terms of intensities for the *001* and *10* peaks, which can be easily understood as revealing the presence of a range of crystallites other than the selected one (i.e., three stacked layers with L_a = 1 nm), therefore providing a distribution of L_a size and of layer number per stack.

To summarize, both the precursor types are highly cross-linked as any non-graphitizable material, and the limited carbonization temperatures suggested that the materials developed graphene crystallites with less than five layers (as confirmed by the HRTEM images to be shown below) and L_a < 3 nm. They might contain isolated graphenes, which would contribute to the background mostly at low 2θ angle as well as domains with L_a < 1 nm, whatever the number of layers is. This cannot be ascertained since the related intensity cannot be easily discriminated from the "regular" background (see Section 2.2). On the other hand, nanosized graphene crystallites developed, with 2 to 4 stacked layers. From them, only the crystallites with three layers are specifically seen as generating the 13° peak because, for the crystallites with an even number of layers (two and four), interference effects are destructive. This is why the 13° peak is specific to poorly organised graphenic carbons. We propose to designate this peak as a small graphene crystallite (SGC) peak. Should the carbonization temperature be increased beyond 1800 °C, crystallites would increase in L_a and layer number, resulting in making the 13° peak vanish as the material nanotexture improves.

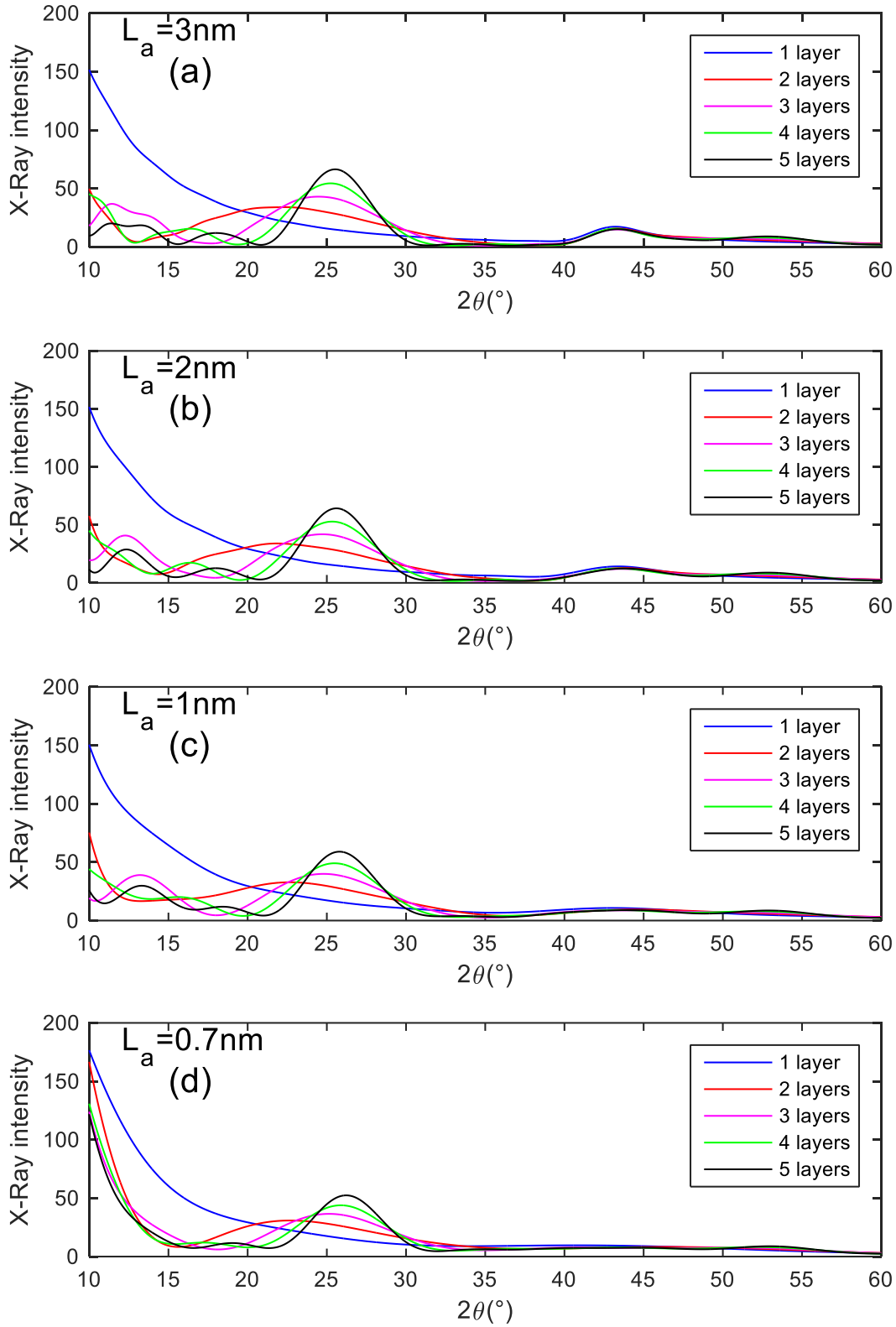

Figure 3. Simulated X-ray diffraction patterns for turbostratic carbon crystallites with the same L_a and a number of graphenes varying from 1 to 5. (**a**–**d**) L_a equals 3, 2, 1, and 0.7 nm, respectively. Each curve corresponds to an average of 10 different configurations (random sequences of plane rotations and positions). The intensity is per carbon atom.

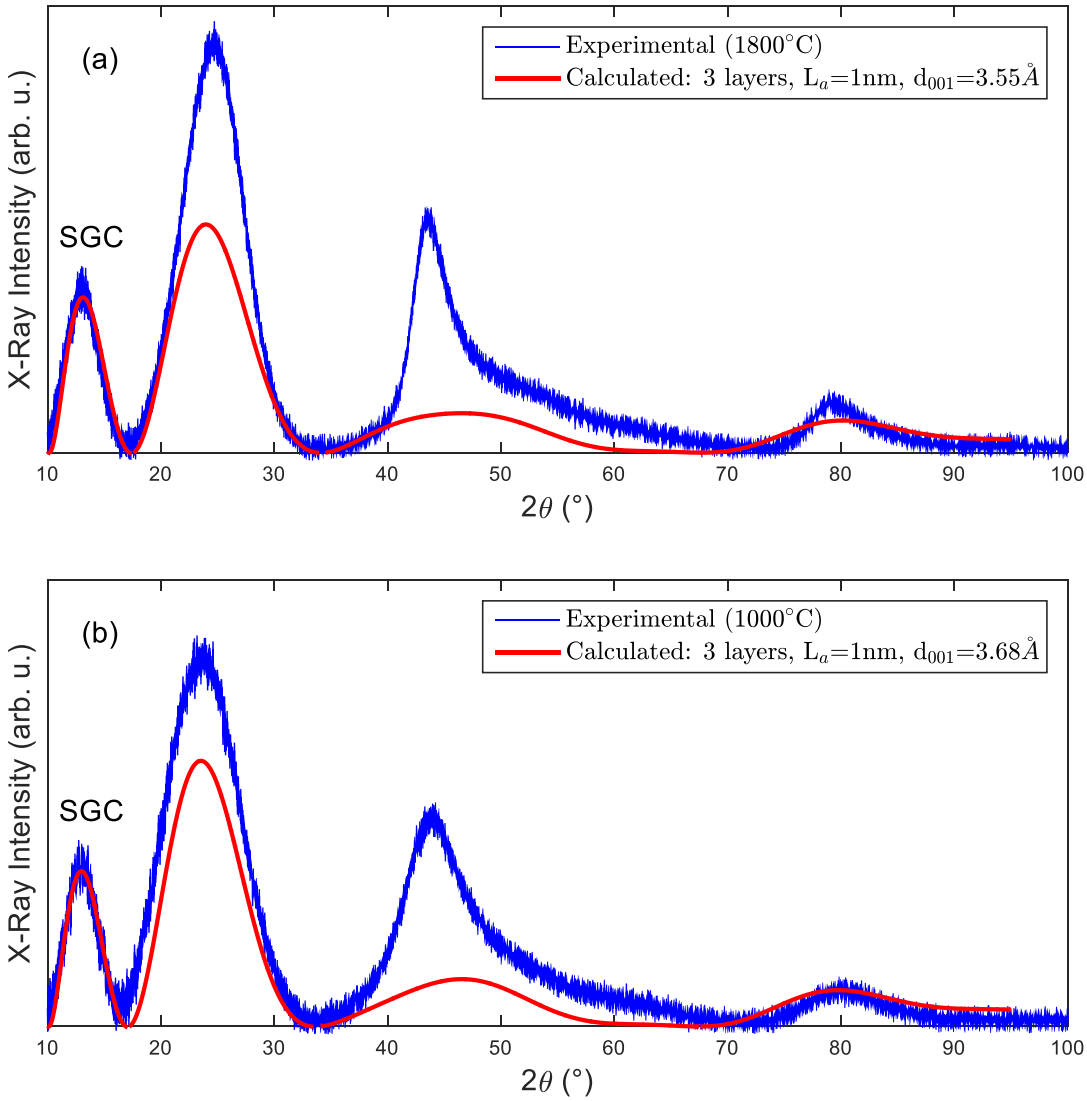

Figure 4. Calculated X-ray diffraction patterns after background removal (red lines) and experimental patterns after background removal normalised to the small graphene crystallite (SGC) peak (blue, noisy lines). The position of the SGC peak is dependent on L_a. (**a**,**b**) correspond to the samples annealed at 1800 and 1000 °C, respectively.

3.2. Raman Spectroscopy

Using two wavelengths, we experimentally determined the α value in Equations (2) and (3). We found 0.731 and 1.131 for samples annealed at 1000 and 1800 °C, respectively.

3.2.1. Raman Spectra Fitted with Two Bands (D and G Only)

The first-order (800–1736 cm^{-1} range) Raman spectra of both cellulose chars are shown in Figure 5, exhibiting the regular D and G bands at about 1340 cm^{-1} and 1594 cm^{-1}, respectively, fitted with two bands. Both bands are broad, which is characteristic of disordered graphenic carbons, but sharpen when the carbonisation temperature is increased (from 1000 to 1800 °C). Another notable feature is a corresponding double intensification of the D band whilst the G band increases by ~50% only. The intensity increases due to the increase in graphenic domain size, leading to a more resonant behavior.

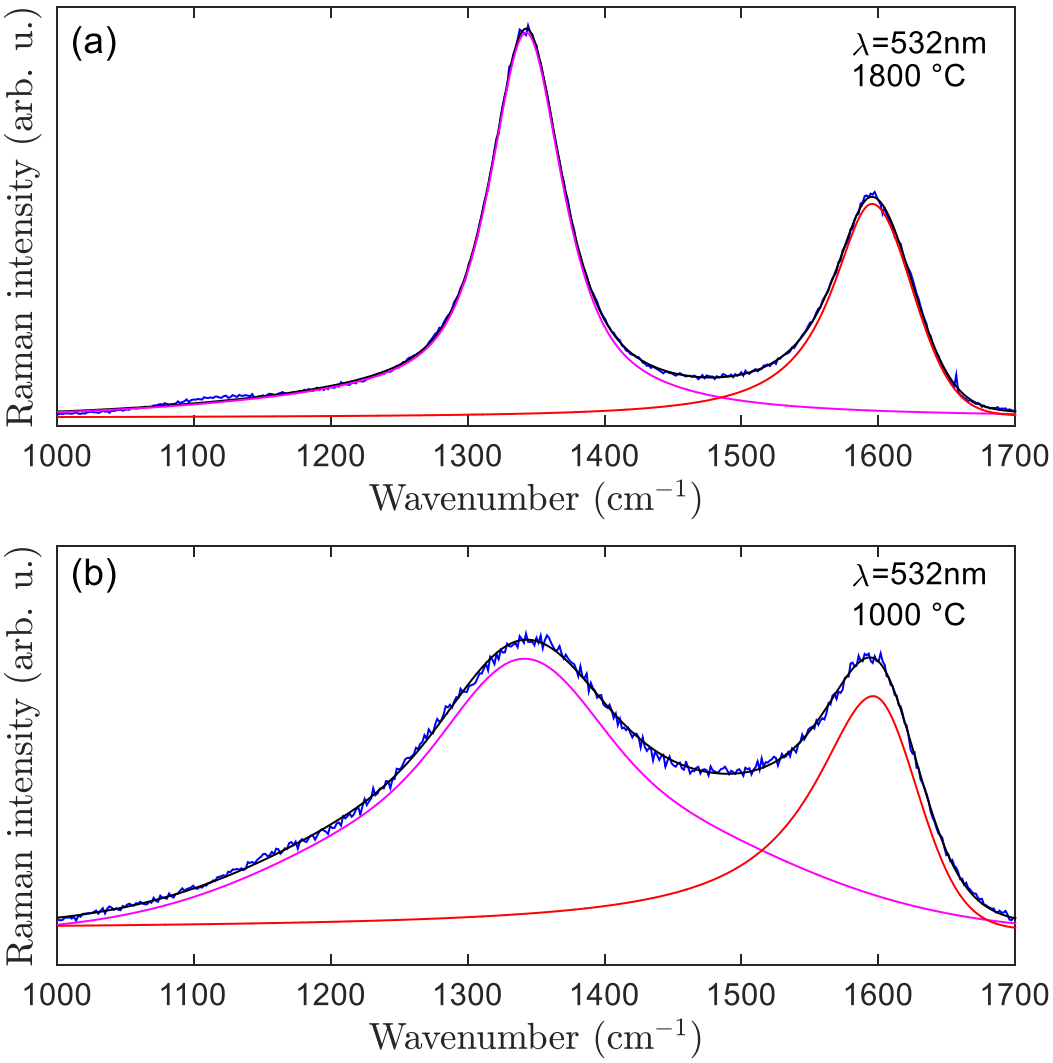

Figure 5. Raman spectra of cellulose carbonized at (**a**) 1800 and (**b**) 1000 °C obtained with an excitation wavelength of 532 nm and fitted with two bands. The magenta lines in both spectra are the result from the fitting of the D band with two components D_s and D_b, as described in Section 2.4.1.

Fitting with two bands, as shown in Figure 5, helps to obtain the intensity of the G and D bands, as well as the full-width at half maximum of the D band ($FWHM_D$). Table 4 lists the average L_a of the crystallites in both cellulose chars calculated from the D and G bands, following the various ways described in Section 2.4. The values obtained from the intensity ratio I_D/I_G are in the order of 1.42 and 2.45 nm at 1000 and 1800 °C, respectively, whereas the L_a values derived from the confinement model using $FWHM_D$ are much higher with a factor of 2 and 3.5, respectively.

Table 4. L_a obtained using the 532 nm excitation wavelength.

Crystallite Size (nm)	1000 °C, 2 °C/min	1800 °C, 2 °C/min
L_a [19]	-	2.45
L_a [22]	1.42	-
L_a [36]	<2.84	8.69

The monotonic increase in L_a for disordered carbons with heat-treatment temperature is obvious and has been reported recurrently in the literature [19,41,50,51]

The D and G bands are significantly broader at low carbonisation temperatures, as a result of the confinement effect at the nanoscale [51]. Because the resonant behavior varies in function of the crystallite size [35], a signal originating from the large crystallites obtained at higher temperatures in a material can dominate the D-band region. Moreover, XRD and Raman do not measure the same characteristics. Indeed, L_a sizes measured by XRD involve distortion-free graphenes (because the XRD peaks result from the X-photons scattered strictly in the same direction of space by the atoms), even though the graphene lattice may be somehow defective (i.e., the graphenes may contain in-plane defects, such as 5–7 ring pairs (so-called Dienes defect [52] or vacancies—which do not alter their planarity)). On the other hand, L_a sizes measured by Raman are not affected by corrugations (long-range angular distortions), providing that the graphene lattice is free of any defect, because each in-plane defect (not only the graphene edges) acts as a scattering site for the electron–hole pairs involved in the double resonance Raman process, travelling across the graphene layers. Thus, complementary information is available with these two techniques.

3.2.2. Raman Spectra Fitted with 5 Bands

Figure 6 shows further analysis of the Raman spectra through fitting them with five bands:

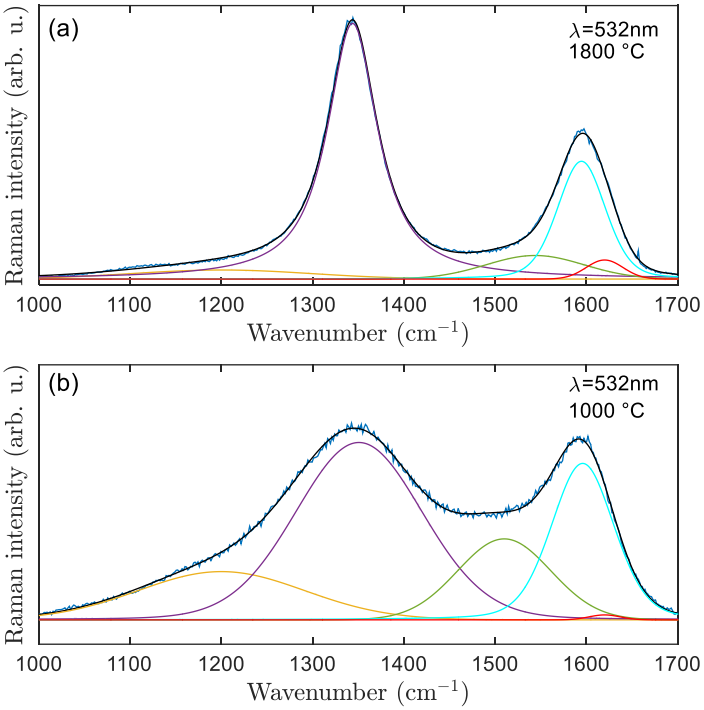

Figure 6. Raman spectra of cellulose carbonized at (**a**) 1800 and (**b**) 1000 °C obtained with an excitation wavelength of 532 nm, and fitted with 5 bands (see Table 2): D_1 (purple) and G (blue), added with D_2 (red), D_3 (green), and D_4 (yellow).

Three additional bands were added to the D_1 and G bands, namely the D_2, D_3, and D_4 bands. Though it is presumably possible to fix the wavenumbers with a set of samples from the same organic origin, it is impossible to do so here as it leads to a less accurate decomposition. The D_3 band at 1510 and 1543 cm^{-1} (for 1000 and 1800 °C carbonisation temperatures, respectively) relates to unstructured (amorphous) carbon. We chose to only discuss the intensity ratio $\frac{ID_3}{I_{total}}$ for quantifying disorders based on our previous studies on biochar materials [29]. From the $\frac{ID_3}{I_{total}}$ ratio in Table 5, we can note that it decreases by a factor of three, accompanied by a proportional decrease in the height of the interband

valley, as seen in Figure 6, when the annealing temperature increases from 1000 to 1800 °C. Likewise for the integrated intensity ratio, which decreases by a factor of about 2. The G-band position (1595 cm^{-1}) remains almost unchanged at both temperatures, whilst the D-band is redshifted from 1350 cm^{-1} to 1343 cm^{-1} when the carbonisation temperature increases. The formation of short-ordered turbostratic graphenic stacks was consistent with literature findings [29,53]. In summary, the band position should be adjusted at each temperature and the valley between the D and G band can be accounted for through the D_3 band. By leaving the wavenumber position of the D_3 band free to adjust, the D_3 band may be considered as a good indicator for disorders.

Table 5. Intensity ratios obtained using the 532-nm excitation wavelength.

Excitation Wavelength 532 nm	1000 °C, 2 °C/min	1800 °C, 2 °C/min
Intensities: $\frac{ID_3}{I_{total}}$	0.173	0.055
Integrated intensities: $\frac{AD_3}{A_{total}}$	0.153	0.08

3.3. HRTEM Image Filtering Analysis, Fringe Analysis

Figure 7 provides an example of HRTEM images of the carbonized cellulose for both carbonization temperatures and the associated filtered images for a distance of 3.4 ± 0.4 Å.

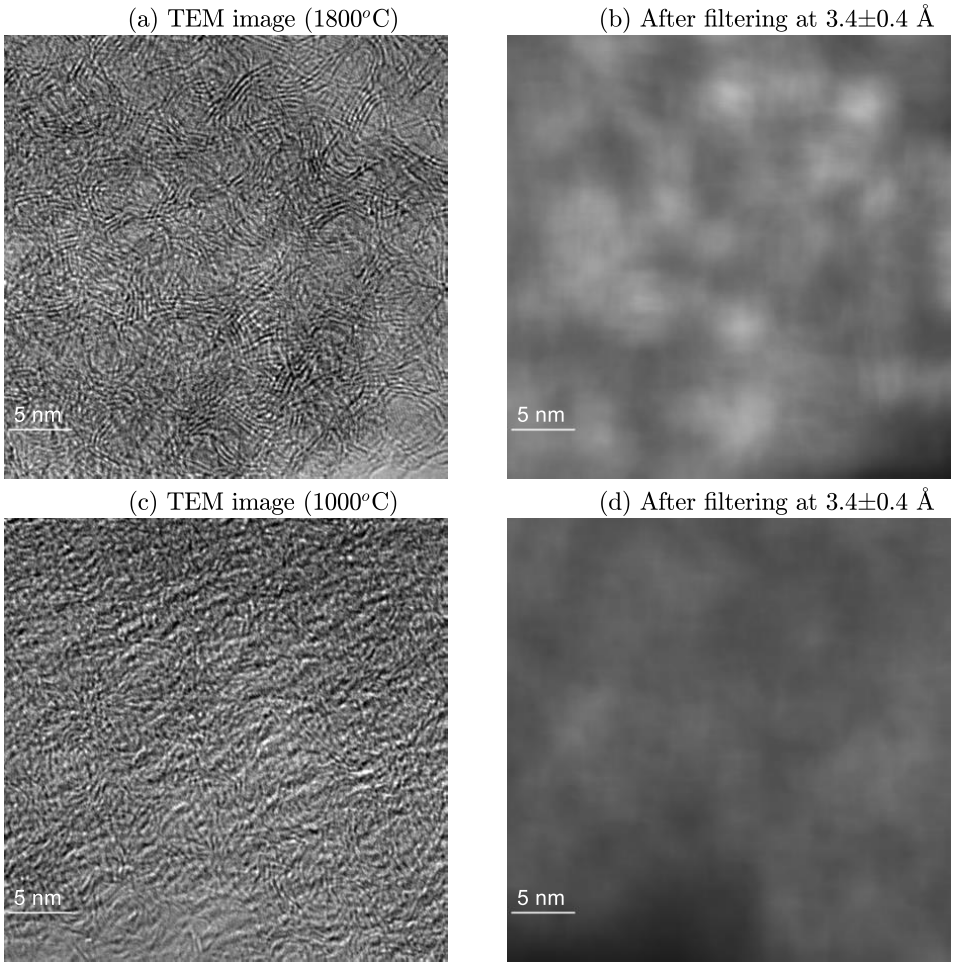

Figure 7. Raw HRTEM images of the cellulose chars (**a**) at 1800 °C, and (**c**) at 1800 °C. (**b**,**d**): associated filtered images.

Comparing Figure 7a,c, it can be seen that, for the cellulose carbonized at 1000 °C, there are fewer graphene sheets. This confirms the transition from a poorly organised material with a short-range ordering of the graphene sheets to a material with improved ordering. When the temperature is increased up to 1800 °C, the graphenes become more apparent because they tend to be larger and their planarity is better; hence, the scattered intensity increases as the number of atoms involved in a single domain increase. The material evolves with a very much larger proportion of curved domains. This is consistent with the merging process of basic structural units [8], which involve straight graphenic planes, but whose merging does not necessarily result in straight domains as it may come with the creation of in-plane defects and local constraints which both affect the planarity. The process is enhanced by the overall effect of increasing the carbonisation temperature which promotes the mobility of atoms in the solid. Although it was chosen not to extract fringe length values from the HRTEM images because the TEM projection of superimposed small domains shorten the associated fringes, which are thus unrepresentative of the sample (see Section 2.5), it is obvious that the lattice fringes increase in length with the increasing temperature, as seen with the TEM images of Figure 7a,c. The average pixel values of the filtered images (Figure 7b,d) are 78 and 114 for the samples annealed at 1000 and 1800 °C, respectively. The increase in the occurrence of 3.4 Å spacing proves that the crystallinity increases, which is fully consistent with the background reduction in XRD.

4. Merging All the Data

Considering all the techniques used in this study, the crystallite size, L_a, as summarized in Table 6, distributes over a range.

Table 6. L_a values obtained directly from XRD (top line), and then from the I_D/I_G obtained by Raman spectroscopy using various correlations available in the literature.

Crystallite Size (nm)	1000 °C, 2 °C/min	1800 °C, 2 °C/min
L_a (XRD)	~1.8	2.8–3.2
L_a [19]	-	~2.5
L_a [22]	1.4	-
L_a [36]	<2.8	8.7

Although L_a is an important indicator of the development of the graphenic domains, none of the L_a obtained should be taken as a universal value because the different techniques do not measure the same feature. L_a obtained from XRD is strictly dependent on the planarity of the graphene. Moreover, we showed that several sizes are visible in the X-ray diffraction patterns. Hence, it is a direct measurement of the average in-plane dimension of the parallel coherent graphene stacks (the genuine crystallites). Should a defect be present in the in-plane graphene lattice while not deforming significantly the orientation of the graphene involved (as for defects such as 5–7 pairs or vacancies for instance), the L_a, as seen by XRD, will not be affected. For the Raman, the "L_a" designation, which is initially a crystallographic term, is not appropriate. This is because the intensity of the D band owes to the amount of both the defects peripheral to the graphenes and the local in-plane defects in the graphene lattice, whereas the G band can manifest even in the absence of graphene because sp^2 carbon chains can also give rise to it. This implies that L_a from Raman not only depends on the in-plane graphene dimension (which is inversely proportional to the number of peripheral defects), but also on the occurrence of local defects dispersed throughout the graphene lattice. The more defective the cellulose-derived carbons are, the more broadened the D band becomes. However, this is not always true in terms of intensity due to the resonance effect and change in behavior around L_a = 2 nm. When the domains are large, the linewidth of the D band is a partial indication of the size of the graphenes involved in the domains, but it can be used more precisely within a sample set to monitor the removal of both the in-plane and peripheral defects with the increasing carbonization temperature. The narrower the D band, the larger the in-plane graphene

dimension even with distortion. The higher L_a values obtained from Raman (through the confinement model) with respect to XRD are a result of the overall presence of distortions in the graphenes at 1000 °C, followed by the structural improvement in the graphene sheets due to the healing of local (in-lattice) defects, to which the Raman signal is sensitive whilst the XRD signal is not (or less). Table 6 shows that both the models of Tuinstra and Koenig [19] and Ferrari and Robertson [22] give values closer to that from XRD than the confinement model. This can be understood as follows: their correlations between L_a and I_D/I_G are based on several kinds of samples from various origins and treatments, with L_a determined by X-ray diffraction, leading to an average behavior, eventually not suitable for a specific series of materials. On the contrary, the confinement model [36] does not use XRD data, and was based on studying a homogenous sample series. However, even if other models [25] now also propose to correlate I_D/I_G, and the *FWHMs* of D and G as the confinement model did, no model can account for all the Raman spectra available in the literature so far.

5. Conclusions

Based on HRTEM, cellulose-derived carbons were found to be mainly composed of graphenic crystallites which distribute over a size range, according to XRD and Raman spectroscopy, possibly including ultra-small domains (L_a < 1 nm, contributing to the background of the XRD patterns), but with a prevalence of small domains (revealed by the *10* and 13° peaks of X-ray diffractograms), and some larger distorted domains for the sample annealed at 1800 °C (revealed by Raman spectroscopy and HRTEM). After an annealing at 1000 °C, the crystallites are distributed according to an isotropic texture, even at a short distance, which means that the areas of similar orientation of the graphenes inherited from the local molecular orientation event which took place during the primary carbonization step are very limited in size. Upon further carbonization, the textural isotropy remained because initial misorientations were too large to be healable. At the employed carbonization conditions (a temperature increase from 1000 to 1800 °C), the resulting materials comprise a minor proportion of carbon atoms not involved in the graphenic crystallites, and hence, are probably involved at the grain boundaries between them and assimilated to an amorphous carbon phase, the amount of which decreases with temperature (based on the evolution of the D_3 band from Raman spectroscopy). Meanwhile, the in-plane extension of graphene lattices, yet curved and distorted, increased from ~2.8 to ~8.7 nm with the increasing temperature (based on the pseudo-L_a calculated from the Raman based on the confinement model), mostly because of the healing of some of the defects, both local (in-lattice) and peripheral. On the nanotextural level, the pronounced (short-radius) curvatures impeded the development of large graphene crystallites. Correspondingly, the genuine L_a (according to its crystallographic definition, i.e., the dimension of the average crystallite across the basal plane) only increased from ~2 to 3 nm with the increasing temperature (based on XRD), mostly because of the healing of small-angle distortions. The stacking configuration within the graphene crystallites is random even at 1800 °C, meaning that the crystallographic structure is turbostratic, and from the textural characteristics (unhealable overall isotropy), it can be predicted that it will remain so for any further temperature increase, up to 3000 °C [8,54].

An important conclusion of the work is that the XRD peak corresponding to a scattering angle of ~13° (Cu X-ray source), the origin of which was not understood in the literature so far, is now fully explained. It is specifically due to crystallites involving an odd but limited number (typically three) of carbon layers with L_a in the range 1–2 nm. It does not mean that this presence is exclusive, and crystallites with an even number of layers (two and four) may be present as well, although destructive interference effects do not allow them contributing to the 13° peak. Therefore, the 13° peak, designated in this study as a small graphene–crystallite (SGC) peak, is not a mark for amorphous carbon, but a mark of poorly organized graphenic carbon (i.e., with low nanotexture).

Overall, the study illustrates that technique, such as XRD, Raman, and HRTEM do not quantify the same material characteristics, although, because of the poor suitability of the vocabulary commonly used in the literature, it is often believed so. This work has addressed the reasons for such discrepancies, and figuring them out has allowed seeing these techniques as being highly complementary.

Author Contributions: Writing: P.K.M., P.P. and M.M.; Experiments: P.K.M.; Data treatment: P.P. and P.K.M.; Samples preparation: T.B.; Project management: E.W.-H. and A.N. All authors have read and agreed to the published version of the manuscript.

Funding: P.K.M. is supported by an Université Fédérale de Midi-Pyrénées scholarship. The French "Programme Investissements d'Avenir" (ANR-10-LABEX-22-01 SOLSTICE grant) is acknowledged for its support in the work on cellulose carbonization.

Institutional Review Board Statement: Not applicable.

Data Availability Statement: The data presented in this study are available on request from the corresponding authors.

Acknowledgments: We thank N. Ratel-Ramond for his help in X-ray diffraction experiments.

Conflicts of Interest: The authors declare no conflict of interest.

References

1. Chowdhury, Z.; Abd Hamid, S.B.; Das, R.; Hasan, M.R.; Zain, S.; Khalisanni, K.; Uddin, M. Preparation of Carbonaceous Adsorbents from Lignocellulosic Biomass and Their Use in Removal of Contaminants from Aqueous Solution. *BioResources* **2013**, *8*, 6523–6555. [CrossRef]
2. Mohamad Nor, N.; Lau, L.C.; Lee, K.T.; Mohamed, A.R. Synthesis of activated carbon from lignocellulosic biomass and its applications in air pollution control—A review. *J. Environ. Chem. Eng.* **2013**, *1*, 658–666. [CrossRef]
3. Gan, L.; Zhu, J.; Lv, L. Cellulose hydrolysis catalyzed by highly acidic lignin-derived carbonaceous catalyst synthesized via hydrothermal carbonization. *Cellulose* **2017**, *24*, 5327–5339. [CrossRef]
4. Zhang, P.; Gong, Y.; Li, H.; Chen, Z.; Wang, Y. Solvent-free aerobic oxidation of hydrocarbons and alcohols with Pd@N-doped carbon from glucose. *Nat. Commun.* **2013**, *4*, 1593. [CrossRef]
5. Zhang, Z.; Yang, S.; Li, H.; Zan, Y.; Li, X.; Zhu, Y.; Dou, M.; Wang, F. Sustainable Carbonaceous Materials Derived from Biomass as Metal-Free Electrocatalysts. *Adv. Mater.* **2019**, *31*, e1805718. [CrossRef]
6. Herou, S.; Schlee, P.; Jorge, A.B.; Titirici, M. Biomass-derived electrodes for flexible supercapacitors. *Curr. Opin. Green Sustain. Chem.* **2018**, *9*, 18–24. [CrossRef]
7. Li, R.; Zhou, Y.; Li, W.; Zhu, J.; Huang, W. Structure Engineering in Biomass-Derived Carbon Materials for Electrochemical Energy Storage. *Research* **2020**, *2020*, 8685436. [CrossRef]
8. Oberlin, A. Carbonization and graphitization. *Carbon* **1984**, *22*, 521–541. [CrossRef]
9. Monthioux, M. Comments on: "Structure evolution mechanism of highly ordered graphite during carbonization of cellulose nanocrystals" by Eom et al. [Carbon 150 (2019) 142–152]. *Carbon* **2020**, *160*, 405–406. [CrossRef]
10. Fujimoto, H. Theoretical X-ray scattering intensity of carbons with turbostratic stacking and AB stacking structures. *Carbon* **2003**, *41*, 1585–1592. [CrossRef]
11. Puech, P.; Dabrowska, A.; Ratel-Ramond, N.; Vignoles, G.L.; Monthioux, M. New insight on carbonisation and graphitisation mechanisms as obtained from a bottom-up analytical approach of X-ray diffraction patterns. *Carbon* **2019**, *147*, 602–611. [CrossRef]
12. Franklin, R.E.; Randall, J.T. Crystallite growth in graphitizing and non-graphitizing carbons. *Proc. R. Soc. Lond. Ser. A Math. Phys. Sci.* **1951**, *209*, 196–218.
13. Gutierrez-Pardo, A.; Ramirez-Rico, J.; Cabezas-Rodríguez, R.; Fernández, J. Effect of catalytic graphitization on the electrochemical behavior of wood derived carbons for use in supercapacitors. *J. Power Sources* **2015**, *278*, 18–26. [CrossRef]
14. Maire, J.; Mering, J. Graphitization of soft carbons. *Chem. Phys. Carbon* **1970**, *6*, 125–190.
15. Sembiring, S.; Situmeang, R.; Sembiring, Z. Synthesis and characterization of asphalt composite precursors using amorphous rice husk silica. *Cerâmica* **2019**, *65*, 194–199. [CrossRef]
16. Cançado, L.G.; Takai, K.; Enoki, T.; Endo, M.; Kim, Y.A.; Mizusaki, H.; Jorio, A.; Coelho, L.N.; Magalhães-Paniago, R.; Pimenta, M.A. General equation for the determination of the crystallite size La of nanographite by Raman spectroscopy. *Appl. Phys. Lett.* **2006**, *88*, 163106. [CrossRef]
17. Pimenta, M.A.; Dresselhaus, G.; Dresselhaus, M.S.; Cançado, L.G.; Jorio, A.; Saito, R. Studying disorder in graphite-based systems by Raman spectroscopy. *Phys. Chem. Chem. Phys.* **2007**, *9*, 1276–1290. [CrossRef]
18. Puech, P.; Kandara, M.; Paredes, G.; Moulin, L.; Weiss-Hortala, E.; Kundu, A.; Ratel-Ramond, N.; Plewa, J.-M.; Pellenq, R.; Monthioux, M. Analyzing the Raman Spectra of Graphenic Carbon Materials from Kerogens to Nanotubes: What Type of Information Can Be Extracted from Defect Bands? *C* **2019**, *5*, 69. [CrossRef]

19. Tuinstra, F.; Koenig, J. Raman Spectrum of Graphite. *J. Chem. Phys.* **1970**, *53*, 1126–1130. [CrossRef]
20. Sadezky, A.; Muckenhuber, H.; Grothe, H.; Niessner, R.; Pöschl, U. Raman microspectroscopy of soot and related carbonaceous materials: Spectral analysis and structural information. *Carbon* **2005**, *8*, 1731–1742. [CrossRef]
21. Zickler, G.; Smarsly, B.; Gierlinger, N.; Peterlik, H.; Paris, O. A Reconsideration of the Relationship Between the Crystallite Size La of Carbons Determined by X-ray Diffraction and Raman Spectroscopy. *Carbon* **2006**, *44*, 3239–3246. [CrossRef]
22. Ferrari, A.C.; Robertson, J. Interpretation of Raman spectra of disordered and amorphous carbon. *Phys. Rev. B* **2000**, *61*, 14095–14107. [CrossRef]
23. Ager, J.W.; Veirs, D.K.; Shamir, J.; Rosenblatt, G.M. Laser heating effects in the characterization of carbon fibers by Raman spectroscopy. *J. Appl. Phys.* **1990**, *68*, 3598–3608. [CrossRef]
24. Matthews, M.J.; Pimenta, M.A.; Dresselhaus, G.; Dresselhaus, M.S.; Endo, M. Origin of dispersive effects of the Raman D band in carbon materials. *Phys. Rev. B* **1999**, *59*, R6585–R6588. [CrossRef]
25. Cançado, L.G.; Da Silva, M.G.; Ferreira, E.H.M.; Hof, F.; Kampioti, K.; Huang, K.; Jorio, A. Disentangling contributions of point and line defects in the Raman spectra of graphene-related materials. *2D Mater.* **2017**, *4*, 025039. [CrossRef]
26. Cuesta, A.; Dhamelincourt, P.; Laureyns, J.; Martínez-Alonso, A.; Tascón, J.M.D. Raman microprobe studies on carbon materials. *Carbon* **1994**, *32*, 1523–1532. [CrossRef]
27. Beyssac, O.; Goffé, B.; Petitet, J.-P.; Froigneux, E.; Moreau, M.; Rouzaud, J.-N. On the characterization of disordered and heterogeneous carbonaceous materials by Raman spectroscopy. Georaman 2002, Fifth International Conference on Raman Spectroscopy. *Appl. Earth Sci.* **2003**, *59*, 2267–2276.
28. Couzi, M.; Bruneel, J.-L.; Talaga, D.; Bokobza, L. A multi wavelength Raman scattering study of defective graphitic carbon materials: The first order Raman spectra revisited. *Carbon* **2016**, *107*, 388–394. [CrossRef]
29. Berhanu, S.; Hervy, M.; Weiss-Hortala, E.; Proudhon, H.; Berger, M.-H.; Chesnaud, A.; Faessel, M.; King, A.; Pham Minh, D.; Villot, A.; et al. Advanced characterization unravels the structure and reactivity of wood-based chars. *J. Anal. Appl. Pyrolysis* **2018**, *130*, 79–89. [CrossRef]
30. Harris, P.J.F.; Tsang, S.C. High-resolution electron microscopy studies of non-graphitizing carbons. *Philos. Mag. A* **1997**, *76*, 667–677. [CrossRef]
31. Singh, M.; Vander Wal, R.L. Nanostructure Quantification of Carbon Blacks. *C* **2019**, *5*, 2. [CrossRef]
32. Monthioux, M.; Noé, L.; Kobylko, M.; Wang, Y.; Cazares-Huerta, T.C.; Pénicaud, A. Determining the structure of graphene-based flakes from their morphotype. *Carbon* **2017**, *115*, 128–133. [CrossRef]
33. Lutterotti, L.; Scardi, P. Simultaneous structure and size–strain refinement by the Rietveld method. *J. Appl. Crystallogr.* **1990**, *23*, 246–252. [CrossRef]
34. Neverov, V.S. XaNSoNS: GPU-accelerated simulator of diffraction patterns of nanoparticles. *SoftwareX* **2017**, *6*, 63–68. [CrossRef]
35. Mallet-Ladeira, P.; Puech, P.; Weisbecker, P.; Vignoles, G.L.; Monthioux, M. Behavior of Raman D band for pyrocarbons with crystallite size in the 2–5 nm range. *Appl. Phys. A* **2014**, *114*, 759–763. [CrossRef]
36. Puech, P.; Plewa, J.-M.; Mallet-Ladeira, P.; Monthioux, M. Spatial confinement model applied to phonons in disordered graphene-based carbons. *Carbon* **2016**, *105*, 275–281. [CrossRef]
37. Cançado, L.G.; Jorio, A.; Pimenta, M.A. Measuring the absolute Raman cross section of nanographites as a function of laser energy and crystallite size. *Phys. Rev. B* **2007**, *76*, 064304. [CrossRef]
38. Asadullah, M.; Zhang, S.; Min, Z.; Yimsiri, P.; Li, C.-Z. Effects of biomass char structure on its gasification reactivity. *Bioresour. Technol.* **2010**, *101*, 7935–7943. [CrossRef] [PubMed]
39. Li, X.; Hayashi, J.I.; Li, C.Z. FT-Raman spectroscopic study of the evolution of char structure during the pyrolysis of a Victorian brown coal. *Fuel* **2006**, *85*, 1700–1707. [CrossRef]
40. Kang, D.S.; Lee, S.M.; Lee, S.H.; Roh, J.S. X-ray diffraction analysis of the crystallinity of phenolic resin-derived carbon as a function of the heating rate during the carbonization process. *Carbon Lett.* **2018**, *27*, 108–111.
41. Kercher, A.; Nagle, D. Microstructural Evolution during Charcoal Carbonization by X-ray Diffraction Analysis. *Carbon* **2003**, *41*, 15–27. [CrossRef]
42. Keiluweit, M.; Nico, P.S.; Johnson, M.G.; Kleber, M. Dynamic Molecular Structure of Plant Biomass-Derived Black Carbon (Biochar). *Environ. Sci. Technol.* **2010**, *44*, 1247–1253. [CrossRef] [PubMed]
43. Dahbi, M.; Kiso, M.; Kubota, K.; Horiba, T.; Chafik, T.; Hida, K.; Matsuyama, T.; Komaba, S. Synthesis of hard carbon from argan shells for Na-ion batteries. *J. Mater. Chem. A* **2017**, *5*, 9917–9928. [CrossRef]
44. Campos-Delgado, J.; Kim, Y.A.; Hayashi, T.; Morelos-Gómez, A.; Hofmann, M.; Muramatsu, H.; Endo, M.; Terrones, H.; Shull, R.D.; Dresselhaus, M.S.; et al. Thermal stability studies of CVD-grown graphene nanoribbons: Defect annealing and loop formation. *Chem. Phys. Lett.* **2009**, *469*, 177–182. [CrossRef]
45. Garvey, C.J.; Parker, I.H.; Simon, G.P. On the Interpretation of X-ray Diffraction Powder Patterns in Terms of the Nanostructure of Cellulose I Fibres. *Macromol. Chem. Phys.* **2005**, *206*, 1568–1575. [CrossRef]
46. Qiao, Q.; Li, X.; Huang, L. Crystalline Cellulose under Pyrolysis Conditions: The Structure–Property Evolution via Reactive Molecular Dynamics Simulations. *J. Chem. Eng. Data* **2020**, *65*, 360–372. [CrossRef]
47. Kwon, S.-M.; Kim, N.; Cha, D.-S. An investigation on the transition characteristics of the wood cell walls during carbonization. *Wood Sci. Technol.* **2009**, *43*, 487–498. [CrossRef]

48. Meng, Y.; Contescu, C.; Liu, P.; Wang, S.; Lee, S.H.; Guo, J.; Young, T. Understanding the local structure of disordered carbons from cellulose and lignin. *Wood Sci. Technol.* **2021**, *55*, 587–606. [CrossRef]
49. Noda, T.; Inagaki, M. The Structure of Glassy Carbon. *Bull. Chem. Soc. Jpn.* **1964**, *37*, 1534–1538. [CrossRef]
50. Paris, O.; Zollfrank, C.; Zickler, G.A. Decomposition and carbonisation of wood biopolymers—A microstructural study of softwood pyrolysis. *Carbon* **2005**, *43*, 53–66. [CrossRef]
51. Wu, H.; Gakhar, R.; Chen, A.; Lam, S.; Marshall, C.P.; Scarlat, R. Comparative analysis of microstructure and reactive sites for nuclear graphite IG-110 and graphite matrix A3. *J. Nucl. Mater.* **2019**, *528*, 151802. [CrossRef]
52. Monthioux, M.; Charlier, J.-C. Giving credit where credit is due: The Stone–(Thrower)–Wales designation revisited. *Carbon* **2014**, *75*, 1–4. [CrossRef]
53. McDonald-Wharry, J.; Manley-Harris, M.; Pickering, K.L. Carbonisation of biomass-derived chars and the thermal reduction of a graphene oxide sample studied using Raman spectroscopy. *Carbon* **2013**, *59*, 383–405. [CrossRef]
54. Ouzilleau, P.; Gheribi, A.E.; Chartrand, P.; Soucy, G.; Monthioux, M. Why some carbons may or may not graphitize? The point of view of thermodynamics. *Carbon* **2019**, *149*, 419–435. [CrossRef]